



## RESEARCH ARTICLE

10.1002/2014JD022686

## Key Points:

- We compare differences between warm-sector and vortex rainstorms in north China
- High-resolution rain gauge and Doppler radar data are used in mesoscale analysis
- Shallow convection produces heavy rainfall in warm sector with much liquid water

## Correspondence to:

P. Zhao,  
zhaoping@cma.gov.cn

## Citation:

Zhong, L., R. Mu, D. Zhang, P. Zhao, Z. Zhang, and N. Wang (2015), An observational analysis of warm-sector rainfall characteristics associated with the 21 July 2012 Beijing extreme rainfall event, *J. Geophys. Res. Atmos.*, 120, doi:10.1002/2014JD022686.

Received 7 OCT 2014

Accepted 19 MAR 2015

Accepted article online 24 MAR 2015

## An observational analysis of warm-sector rainfall characteristics associated with the 21 July 2012 Beijing extreme rainfall event

Lingzhi Zhong<sup>1</sup>, Rong Mu<sup>2</sup>, Dalin Zhang<sup>3</sup>, Ping Zhao<sup>1</sup>, Zhiqiang Zhang<sup>4</sup>, and Nan Wang<sup>5</sup>

<sup>1</sup>State Key Laboratory of Severe Weather, Chinese Academy of Meteorological Sciences, Beijing, China, <sup>2</sup>Chongqing Meteorological Bureau, Chongqing, China, <sup>3</sup>Department of Atmospheric and Oceanic Science and Center for Scientific Computation and Mathematical Modeling, University of Maryland, College Park, Maryland, USA, <sup>4</sup>National Meteorological Information Center, Beijing, China, <sup>5</sup>Shanxi Meteorological Observatory, Shanxi, China

**Abstract** An observational analysis of the multiscale processes leading to the extreme rainfall event in Beijing on 21 July 2012 is performed using rain gauge records, Doppler radar, and satellite products, radiosondes, and atmospheric analysis. This rainstorm process included two heavy rainfall stages in the early afternoon [1300–1400 Beijing Standard time (BST) (0500–0600 UTC)] and the evening (1600–1900 BST), respectively. The first stage exhibited warm-sector rainfall characteristics as it occurred under low-level warm and moist southeasterly flows ahead of a synoptic-scale vortex and a cold front. When the southeasterly flows turned northeastward along a southwest-northeast oriented mountain range in western Beijing, mesoscale convergence centers formed on the windward side of the mountain range in the early afternoon, initiating moist convection. Radar echo showed a northeastward propagation as these flows extended northward. Despite the shallowness of moist convection in the warm sector, atmospheric liquid water content showed the rapid accumulation, and a large amount of supercooled water and/or ice particles was possibly accumulated above the melting level. These appeared to contribute to the occurrence of the largest rainfall rate. During the second stage, as the synoptic-scale vortex moved across Beijing, with southeastward intrusion of its northwesterly flows, the vortex-associated lifting caused the generation of strong updrafts aloft and formed deep convection. This facilitated the further accumulation of supercooled water and/or ice particles above the melting level. Radar echo propagated southeastward. Liquid water showed a decrease in the lower troposphere, and there were strong downdrafts due to evaporation of liquid water particles, which resulted in the relatively weak hourly rainfall rates.

### 1. Introduction

Summer rainstorms in east China are often dominated by southwesterly or southeasterly monsoonal flows [e.g., *Tao*, 1981; *Chen et al.*, 1991; *Ding*, 2004; *Zhao et al.*, 2007]. The strong southerly flows transport abundant warm and moist air from tropical oceans and supply sufficient moisture for the development of rainstorms. Moreover, the development and track of extratropical cyclones are also sensitive to moist disturbance [*Cao and Moore*, 1998; *Cao and Zhang*, 2005]. When the southerly flows hit mountains [*Huang et al.*, 1986] or are lifted by “old” cold boundaries associated with previously dissipated mesoscale convective systems (MCSs), there is usually the occurrence of heavy rainfall events [*Zhang and Zhang*, 2012; *Luo et al.*, 2014]. These rainstorms occur within warm and moist air masses with little thermal gradients that are far away from cold fronts, so they are referred to as warm-sector rainstorms [*Nozumi and Arakawa*, 1968; *Tao*, 1981]. The warm-sector rainstorms are found to account for many heavy rainfall events in China [*Tao*, 1981].

There have been numerous studies of warm-sector rainstorms occurring in south China. They are closely related to onsets of southwesterly monsoon or accompanied by low-level southwesterly jets ahead of Meiyu fronts [*Feng and Luo*, 1997; *Xue*, 1999; *Zhou et al.*, 2003]. *Sun et al.* [2002] and *Zhao et al.* [2003] found that the regional topography in south China could play an important role in triggering and maintaining local rainstorms in a warm sector. Based on Doppler radar data and numerical simulations, *Xia et al.* [2006], *Xia and Zhao* [2009], and *Zhang et al.* [2009] found that heavy rainfall tends to appear on the left side of a low-level southwesterly jet, where mass convergence and lifting are peaked. Of interest is that warm-sector and frontal rainstorms may coexist over south China, which often forms two rainbelts [*Zhao et al.*, 2008]. The warm-sector rainbelt, typically 200–300 km away from a quasi-stationary front,

©2015. The Authors.

This is an open access article under the terms of the Creative Commons Attribution-NonCommercial-NoDerivs License, which permits use and distribution in any medium, provided the original work is properly cited, the use is non-commercial and no modifications or adaptations are made.

could generate much greater amounts of rainfall than that associated with the frontal rainbelt. Moreover, the frontal rainfall is often accompanied by intrusion of a midlevel dry/cold air mass, and so its secondary circulations normal to the frontal rainbelt are slantwise and driven by moist symmetric instability [Zhang and Ni, 2009]. On the other hand, secondary circulations associated with the warm-sector rainstorm are upright and maintained by moist convective instability.

In contrast, rainstorms in north China are usually associated with cold frontal systems [Tao, 1981] and a dry and cold intrusion from upper levels into the warm and moist sector in the lower troposphere [Gao *et al.*, 2010], and seldom occur in the warm sector. This hinders a better understanding and prediction of heavy rainfall events associated with warm-sector rainstorms in north China. On 21 July 2012, however, the heaviest daily total rainfall since 1976 occurred in Beijing and the adjacent areas. This rainstorm event had a regional average of 190.3 mm (far more than the climatological mean of 160.5 mm in July) in the Beijing area and an amount of 24 h accumulated 460 mm (nearly equal to the local annual precipitation of 542 mm) and an hourly rainfall above 85 mm in the western mountain area of Beijing [Zhang *et al.*, 2013; Zhou *et al.*, 2013]. Some studies showed that this rainstorm consisted of two different stages: the first prefrontal heavy rainfall stage with topographical lifting, easterly winds in the local early afternoon, and northwesterly winds in the local evening; and the second frontal but relatively weak rainfall stage at night, as a large-scale cold front approached Beijing [Sun *et al.*, 2013; Zhang *et al.*, 2013]. Because of its high impact and extreme rainfall event, several studies of this Beijing rainstorm have been published [e.g., Chen *et al.*, 2013; Sun *et al.*, 2013; Zhang *et al.*, 2013; Zhao *et al.*, 2013; Du *et al.*, 2014; Jiang *et al.*, 2014; Ran *et al.*, 2014; Xu *et al.*, 2014]. These studies examined the structures and evolutions of large-scale circulation systems (such as an upper troposphere jet, a warm and moist low-level jet, a low-level trough, a cold front, and a shear line) in relation to the extreme event and also explored the possible roles of linear MCSs and radar echo training in generating heavy rainfall. Meanwhile, they paid much attention to differences between the prefrontal (before 2000 BST 21 July) and subsequent frontal stages. The prefrontal stage consisted of two processes. One was characterized by a typical warm-sector rainstorm (occurring under southeasterly flows) in the early afternoon (1300–1400 BST 21 July), with the greatest hourly rainfall amount, and another was associated with intrusions of a low-level vortex and northwesterly flows in the evening (1600–1900 BST 21), with a relatively weak hourly rainfall amount (see sections 3 and 4). However, the previous studies focused on a comparison between the prefrontal and frontal stages instead of that between the warm-sector and vortex-producing rainstorms. Therefore, several questions still remain unanswered. For example, what mesoscale features in atmospheric circulation and cloud/liquid water were associated with the occurrence of the warm-sector heaviest hourly rainfall in the early afternoon? How were they distinguished from those associated with the later vortex-associated rainfall?

In the present study, using hourly rain gauge records and atmospheric analysis data sets, we examine features of synoptic-scale and mesoscale circulations in the warm sector. Using high-resolution radar reflectivity, its derived products, and satellite products, we also analyze mesoscale features of atmospheric circulation, cloud, and atmospheric liquid water. Meanwhile, we compare with those in the vortex-producing rainstorm process. These analyses are helpful to understand differences in mesoscale circulation and cloud/water structures between warm-sector and vortex-producing rainfall processes in north China and to forecast warm-sector heavy rainfall events there. Section 2 describes the data sets and methods used for this study. Section 3 examines the evolutions of rainfall and radar echo. Section 4 presents multiscale structures of atmospheric circulation and features of water vapor transport, cloud, and convection. Section 5 discusses some physical factors responsible for the largest rainfall intensity in the warm sector. A summary and a concluding remark are provided in section 6.

## 2. Data and Methodology

This study utilizes hourly rain gauge data collected at 5163 automated rain gauge stations (Figure 1a) and routine radiosonde temperature data at 0800 BST 21 and 2000 BST in China. The above station data have been under quality control and archived at the National Meteorological Information Centre of China. Following Zhang *et al.* [2013], the National Centers for Environmental Prediction (NCEP) final analysis with a horizontal resolution of  $1^\circ \times 1^\circ$  at a 6 h interval is used to describe atmospheric environmental conditions.

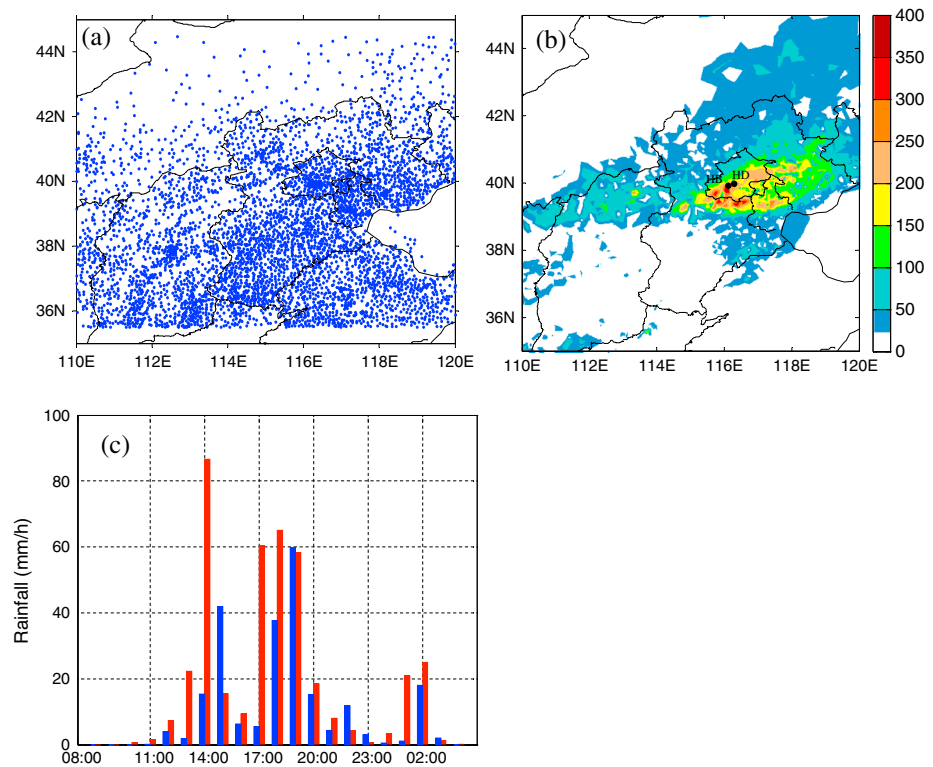


**Figure 1.** (a) Distribution of 5163 rain gauge stations; (b) horizontal map of 24 h (0800 BST 21 to 0800 BST 22) accumulated rainfall (mm) at rain gauge stations, in which positions of Hebei town (HB; with the latitude/longitude of 39.93°N/116.10°E) and Haidian (HD; with the latitude/longitude of 39.98°N/116.28°E) are shown; and (c) hourly rainfall rates ( $\text{mm h}^{-1}$ ) at HB (red) and HD (blue) stations from 0800 BST 21 to 0400 BST 22 July 2012.

High-resolution features of precipitation, mesoscale convective systems, and cloud/liquid water can be clearly exhibited by radar reflectivity and its retrieved products [e.g., Heymsfield, 1979; Amburn and Wolf, 1997; Yamada *et al.*, 2003; Zhou and Zhang, 2005; Zhang *et al.*, 2008, 2012a, 2012b; Zhou, 2009]. In the present study, Doppler weather radar data at Beijing station (with the longitude/latitude of 116.47°E, 39.81°N and the elevation of 92 m above the sea level) with a 10 cm (S band) wavelength, an approximate 1° beam width by a 1 km range resolution, and a volume scan sampling frequency of 6 min are used. Each volume scan consists of nine sweeps, with elevation angles ranging from 0.5° (base scan) to 19.5°. The quality control of the raw radar data is performed by removing noise and ground clutter and correcting Doppler velocity according to the method of Oye *et al.* [1995]. In spite of the data quality control, some noises are occasionally seen in the radar data. The scanned data in the spherical coordinates are then converted into the Cartesian coordinates.

Using the 4-D variational data assimilation (4DVAR) analysis system with a 3-D cloud model developed by Sun and Crook [1997, 1998, 2001], 3-D gridded wind ( $u$ ,  $v$ , and  $w$ ) data are derived from radial velocity of one single-Doppler radar in Beijing. This model contains six prognostic equations, that is, three momentum equations, the thermodynamic equation, the rainwater equation, and the total water equation [Sun and Crook, 1997]. The model physical processes are condensation and evaporation of cloud water, evaporation of raindrops in subsaturated air, autoconversion of cloud to rain, accretion of cloud by rain, and sedimentation of rain. Moreover, the four-dimensional variational data assimilation technique is applied in this analysis system. The objective is to find an initial state that can, upon model integration, produce output parameters matching the observations as closely as possible. In this analysis system, the assimilation of radar reflectivity has little effect on the retrieved horizontal wind [Sun and Crook, 2001]. Some studies have shown that the error of the retrieved horizontal wind from the 4DVAR analysis system is small. For example, when using single-Doppler (dual-Doppler) information, the relative root-mean-square (RMS) error is 12.3% (0.5%) for the retrieved horizontal velocity fields and 9.1% (0.9%) for the retrieved

vertical velocity [Sun and Crook, 1997], and the primary difference between using single- and dual-Doppler data is near 10% [Sun and Crook, 1998]. Crook and Sun [2002] showed that the retrieved wind has a mean vector difference of  $2.6 \text{ m s}^{-1}$  relative to the independent aircraft observations. They also compared with the radar radial velocity, indicating a mean difference of  $2 \text{ m s}^{-1}$  between the radar radial velocity and that calculated from the retrieved wind fields. Moreover, Mu *et al.* [2007] compared the difference of single- and dual-radar retrieved wind fields in northern China using the 4DVAR analysis system. Their results showed the similar features between single- and dual-radar retrieved wind fields. Larger differences mainly appear over some areas where radar echoes are weaker, and the difference between the radar radial velocity and that calculated from the single-radar retrieved wind fields is  $2 \text{ m s}^{-1}$ . Sun *et al.* [2010] examined errors of the retrieved wind fields using the upgraded version of the 4DVAR analysis system and the Doppler radar data at Beijing radar station and its adjacent (Tianjin) radar station. Their sensitivity study with and without the Tianjin data showed that the inclusion of the data did not make much difference to the assimilation analysis. So, the Beijing radar data are only used in their study. Meanwhile, they also showed a mean error of the retrieved wind fields below  $3.5 \text{ m s}^{-1}$  when the single-radar information at Beijing station is assimilated.

Under this study, we run the 4DVAR assimilation analysis system with a horizontal/vertical resolution of  $5 \text{ km}/500 \text{ m}$  at a 6 min interval in a research environment and consider the numerical dynamical cloud model. The sounding data of pressure, temperature, and dew point temperature at Beijing meteorological station (with the identification number 54511, the latitude/longitude  $39.48^\circ\text{N}/116.28^\circ\text{E}$ , and the elevation of  $31.3 \text{ m}$  above the sea level) at 0800 BST 21 July 2012 are used as the initial profiles. Following Sun *et al.* [2010], the single-radar velocity azimuthal display (VAD) profile at Beijing radar station is interpolated onto the 4DVAR grids. The initial horizontal wind fields are calculated from a radar VAD analysis, and the initial vertical velocity is assumed zero. The boundary conditions for the velocities normal to the boundaries are assumed zero, and, for other variables, their derivatives normal to the boundaries are also assumed zero. To evaluate the errors of the retrieved horizontal wind fields, consistent with Crook and Sun [2002], we also calculate the difference between the radar radial velocity and that calculated from the retrieval wind fields for this rainstorm process. Our results show that the RMS error at the height of  $1.5 \text{ km}$  away from the elevation of Beijing radar station is  $1.7 \text{ m s}^{-1}$  for the entire study area. The above analyses imply that the retrieved horizontal velocity above  $4 \text{ m s}^{-1}$  is generally acceptable. In the present study, therefore, we analyze this retrieved wind velocity.

The echo top (hereafter ET) height is calculated using the method of the WSR-88D radar [Maddox *et al.*, 1999; Xiao *et al.*, 2009]. According to the method of Greene and Clark [1971, 1972] and Robert and Yates [1972], the formula of the vertically integrated liquid water content (hereafter VIL) is written as

$$\text{VIL} = 3.44 \times 10^{-6} \times \sum_{i=1}^{N-1} \left( \frac{Z_i + Z_{i+1}}{2} \right)^{\frac{4}{7}} \times \Delta h_i,$$

in which the spectrum of rain drops is assumed as the *M-P* distribution;  $Z_i$  is the 3-D gridded radar reflectivity factor at level  $i$ ;  $\Delta h_i$  is the difference ( $500 \text{ m}$ ) of the height between levels  $i$  and  $i + 1$ ; and  $N$  is the total vertical level number. Using this method, VIL from the surface to the melting level (or  $0^\circ\text{C}$  level) is derived from radar reflectivity. In spite of some uncertainties of these radar retrieved operational products, they have been still extensively applied in analyzing structures and evolutions of convective systems [Amburn and Wolf, 1997; Sun and Crook, 2001; Li *et al.*, 2005; Mu *et al.*, 2007, 2012; Xiao *et al.*, 2008, 2009; Jin *et al.*, 2010; Zhang *et al.*, 2012a, 2012b]. Moreover, black body temperature equivalent (hereafter TBB) data with a horizontal resolution of  $5 \text{ km}$  at a 30 min interval from Chinese Fengyun 2 stationary meteorological satellite are also used to examine cloud features.

To analyze scale-dependent features of a rainstorm, we separate a mesoscale field ( $A'$ ) from the total field ( $A$ ) using a simple mesoscale filter designed by Tao and Xie [1989]. Here  $A' = A - \hat{A}$  and  $\hat{A}$  is for spatial nine-point smoothing values with a smoothing coefficient ( $s$ ) of 0.5 as follows:

$$\begin{aligned} \hat{A}_{i,j} &= A_{i,j} + \frac{s}{2}(1-s)\nabla^2 A_{i,j} + \frac{s^2}{4}(A_{i-1,j-1} + A_{i-1,j+1} + A_{i+1,j+1} + A_{i+1,j-1} - 4A_{i,j}) \\ \nabla^2 A_{i,j} &= A_{i+1,j} + A_{i-1,j} + A_{i,j+1} + A_{i,j-1}. \end{aligned}$$

Their study showed that when this filter is performed three times for the gridded data with a horizontal resolution of  $\leq 100$  km,  $\hat{A}$  remains more than 95% synoptic-scale information (around 2000 km) and  $A'$  remains more than 70% mesoscale information (around 500 km). They applied this filter in analyzing mesoscale features in north China. In the present study, we apply this filter to the NCEP final analysis data set.

Moreover, we use quasi-geostrophic  $\omega$  ( $p$  velocity) equation to quantify  $p$  velocity driven by the synoptic-scale forcing and isolate it from topographic effects. The quasi-geostrophic  $\omega$  equation is written as [Tao and Xie, 1989]

$$\sigma \nabla^2 \omega + f_0^2 \frac{\partial^2 \omega}{\partial p^2} = f_0 \frac{\partial}{\partial p} \left[ \mathbf{V}_g \cdot \nabla \left( \frac{1}{f_0} \nabla^2 \phi + f \right) \right] + \nabla^2 \left[ \mathbf{V}_g \cdot \nabla \left( -\frac{\partial \phi}{\partial p} \right) \right].$$

Here  $\sigma$  is the static stability;  $f$  is the Coriolis parameter;  $f_0$  is the Coriolis parameter at 40°N (near Beijing);  $\phi$  is the geopotential height; and  $\mathbf{V}_g$  is the geostrophic wind. An overrelaxation method is used to solve Poisson equation, in which  $\omega$  is set to zero at 100 hPa. To remove effects of topographic and boundary layer forcings on tropospheric vertical velocity,  $\omega$  is also set to zero at the surface. The  $\hat{A}$  field of the NCEP final analysis is applied to diagnose the  $\omega$  equation.

### 3. Temporal and Spatial Characteristics

Figure 1b shows the 24 h (0800 BST 21 to 0800 BST 22 July) accumulated rainfall map from rain gauge stations. Our statistic result shows that among more than 5000 stations (shown in Figure 1a), there were 4121 stations recording rainfall during this period. A rainy belt of above 100 mm appeared in Beijing and the adjacent areas between 39°N/115°E and 41°N/119°E, with the largest rainfall amount of greater than 400 mm at Hebei town station (hereafter HB; with the latitude/longitude of 39.93°N/116.10°E). Rainfall at HB began at 1000 BST 21, and its rainfall rates increased rapidly afterward (Figure 1c). Hourly rainfall rates exceeded 20 mm during 1200–1300 BST, and the maximum hourly rate of 86.7 mm appeared during 1300–1400 BST (in the early afternoon). During 1500–1600 BST, rainfall rates decreased quickly, below 10 mm. Rainfall rates rapidly increased again from 1600 to 1900 BST (in the evening), up to about 60 mm h<sup>-1</sup> at 1900 BST, and decreased from 1900 to 2300 BST, which indicated the second rainfall process. The third increase in rainfall rates appeared from 0100 to 0200 BST 22, with much weaker rainfall rates relative to those of the first two heavy rainfall periods. A similar time series of rainfall also appeared at Haidian station (hereafter HD; with the latitude/longitude of 39.98°N/116.28°E) (Figure 1c) and Mentougou station (near HB) [see Zhang *et al.*, 2013, Figure 1b]. Because this rainstorm moved eastward, rainfall began later at HD than at HB (Figure 1c). These results indicated three major rainfall stages in Beijing: two heavy rainfall stages in the early afternoon and in the evening, respectively, and one weak rainfall stage at night. It is seen in section 4.1 that a cold front was far away from Beijing in the first stage, appeared to the west of Beijing in the second stage, and passed Beijing in the third stage (belonged to the frontal rainfall).

High-resolution composite radar reflectivity (hereafter CR is for the column maximum reflectivity) shows strong convective cells with reflectivity exceeding 40 dBZ in the southwest of Beijing before 1200 BST 21, with small values (below 35 dBZ) near HB (Figures 2a–2d). Since 1200 BST (Figures 2e and 2f), a northwest-southeast oriented belt of high CR values (with the central value above 45 dBZ) developed in the southwest of Beijing and moved northeastward. By 1400 BST (Figure 2g), this high CR belt moved across HB, and a new CR center appeared near HB again. The development of these large CR values corresponded well to the local heavy rainfall during 1300–1400 BST (shown in Figure 1c). Subsequently, CR decreased near HB at 1500 BST (Figure 2h). Meanwhile, a large area of CR above 40 dBZ appeared to the southwest of Beijing (near 39.5°N/115.5°E) and moved eastward. This strong echo moved across HB during 1600–1900 BST (Figures 2i–2l), which corresponded to heavy rainfall during the evening hours (Figure 1c).

Figure 3 further shows the time-longitude/-latitude cross section of CR along 39.93°N/116.10°E, at which HB is located. High CR belts of greater than 40 dBZ generally began at 116°E, showing three eastward propagation components via HB at different times (Figure 3a). The first eastward propagation component appeared during 1200–1400 BST, also showed a northward propagation component (Figure 3b), and dissipated near 117°E/40.3°N. The second eastward propagation component via HB occurred from 1600 to 2300 BST 21, also showed a southward propagation component, and weakened at 117.6°E/39.2°N.

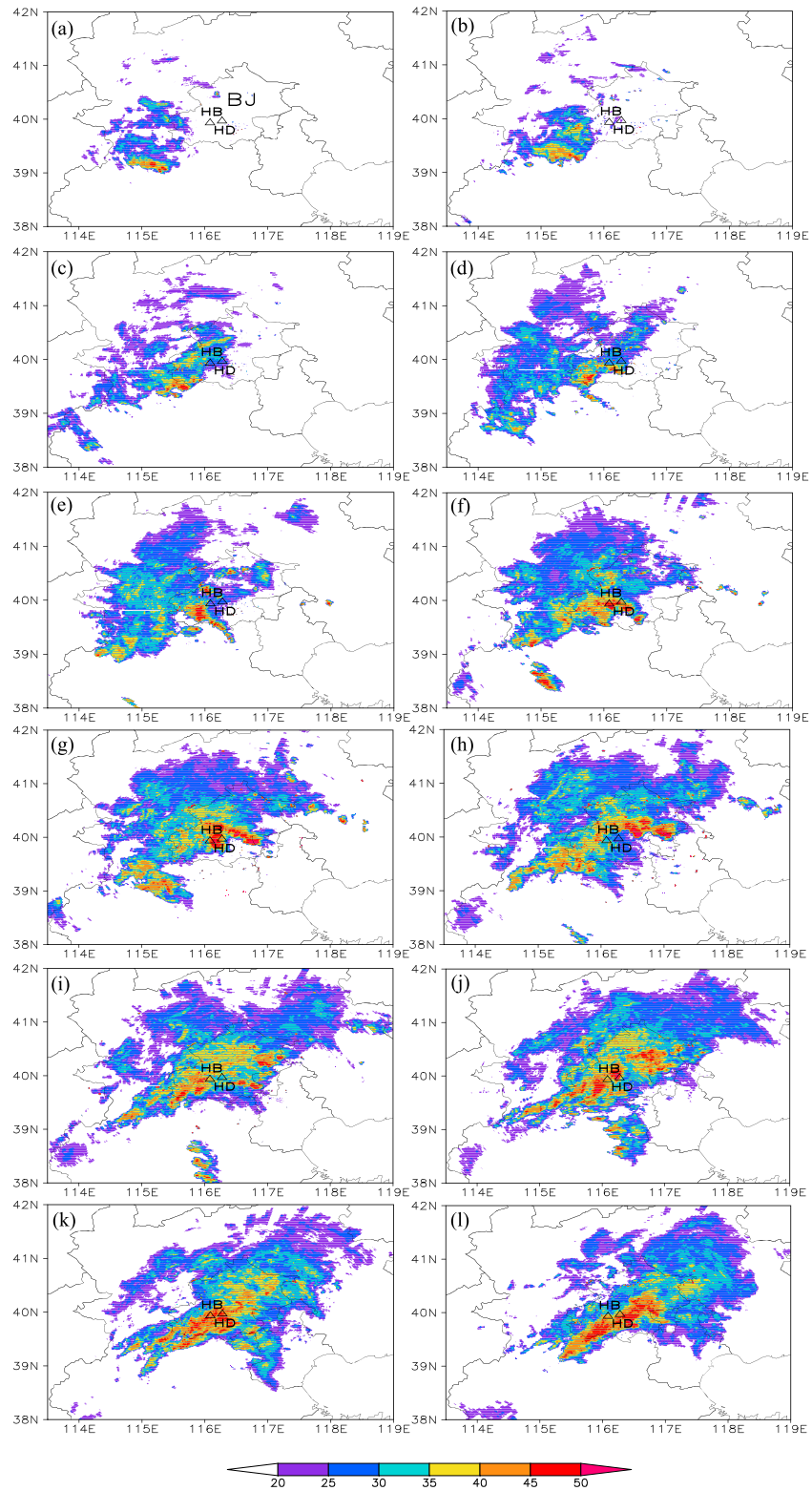


**Figure 2.** Horizontal map of composite radar reflectivity (dBZ) at (a) 0800, (b) 0900, (c) 1000, (d) 1100, (e) 1200, (f) 1300, (g) 1400, (h) 1500, (i) 1600, (j) 1700, (k) 1800, and (l) 1900 BST 21 July. HB and HD denote the stations of Hebei and Haidian, respectively, and in (a) BJ denotes the position of Beijing.

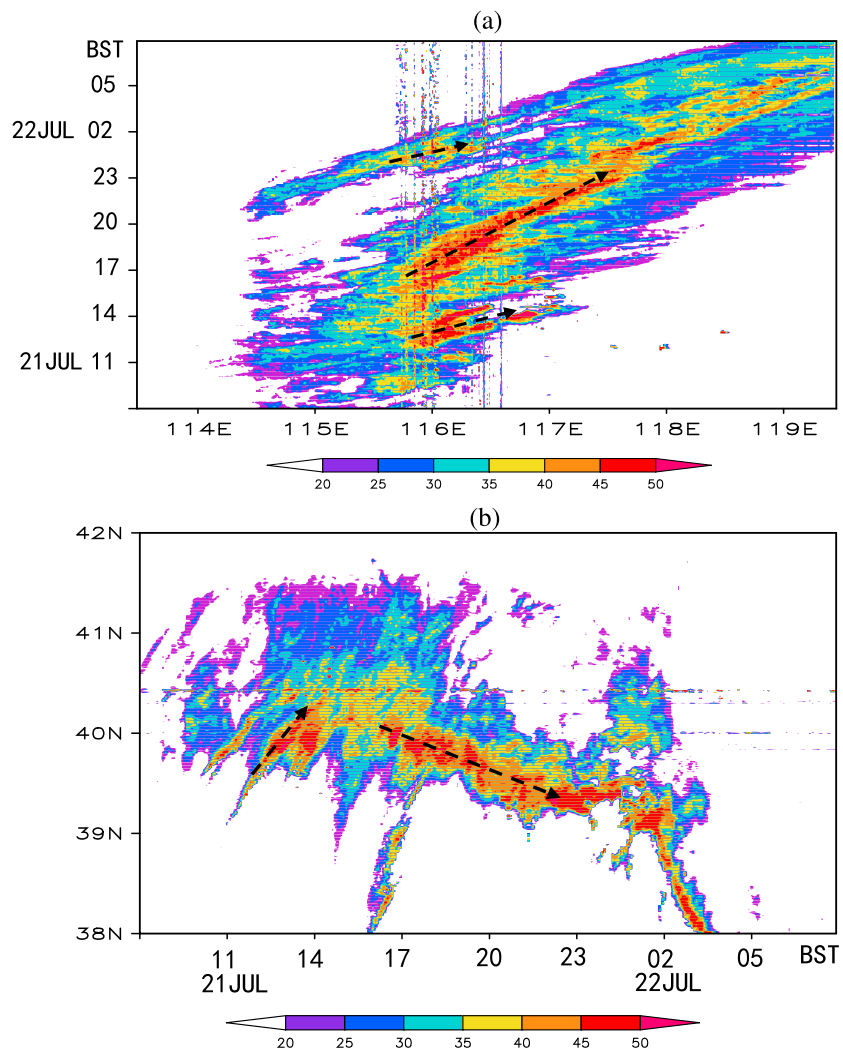


**Figure 3.** (a) Time-longitude cross section of composite radar reflectivity (dBZ) along the latitude  $39.93^{\circ}\text{N}$  from 0800 BST 21 to 0800 BST 22, in which dashed lines with arrows indicate the propagation directions of peak reflectivity; and (b) same as in Figure 3a but along the longitude  $116.10^{\circ}\text{E}$ .

The third eastward propagation component via HB occurred between 2330 BST 21 and 0200 BST 22 (Figure 3a), not showing a remarkably meridional propagation (Figure 3b), which corresponded to the weakest rainfall at HB.

It is evident that for the prefrontal rainstorms from the early afternoon to the evening noted by Zhang *et al.* [2013], radar echo showed two different propagations via HB. From 1200 to 1400 BST, CR strengthened in the southwest of Beijing and then moved northeastward, which coincided with the first heavy rainfall process at HB. From 1600 through 2300 BST 21 July, CR generally showed a systematic southeastward propagation from the west of Beijing via HB and persisted for a long period, which accompanied the second heavy rainfall process at HB in the evening hours. This difference in propagation suggests that the two heavy rainfall scenarios were possibly associated with two different weather systems, which are examined below.

#### 4. Multiscale Analyses

In this section, we analyze synoptic-scale and mesoscale features of atmospheric circulation in the two heavy rainfall processes (in the early afternoon and the evening) using atmospheric analysis data, radar-derived products (such as horizontal and ET), and satellite products.

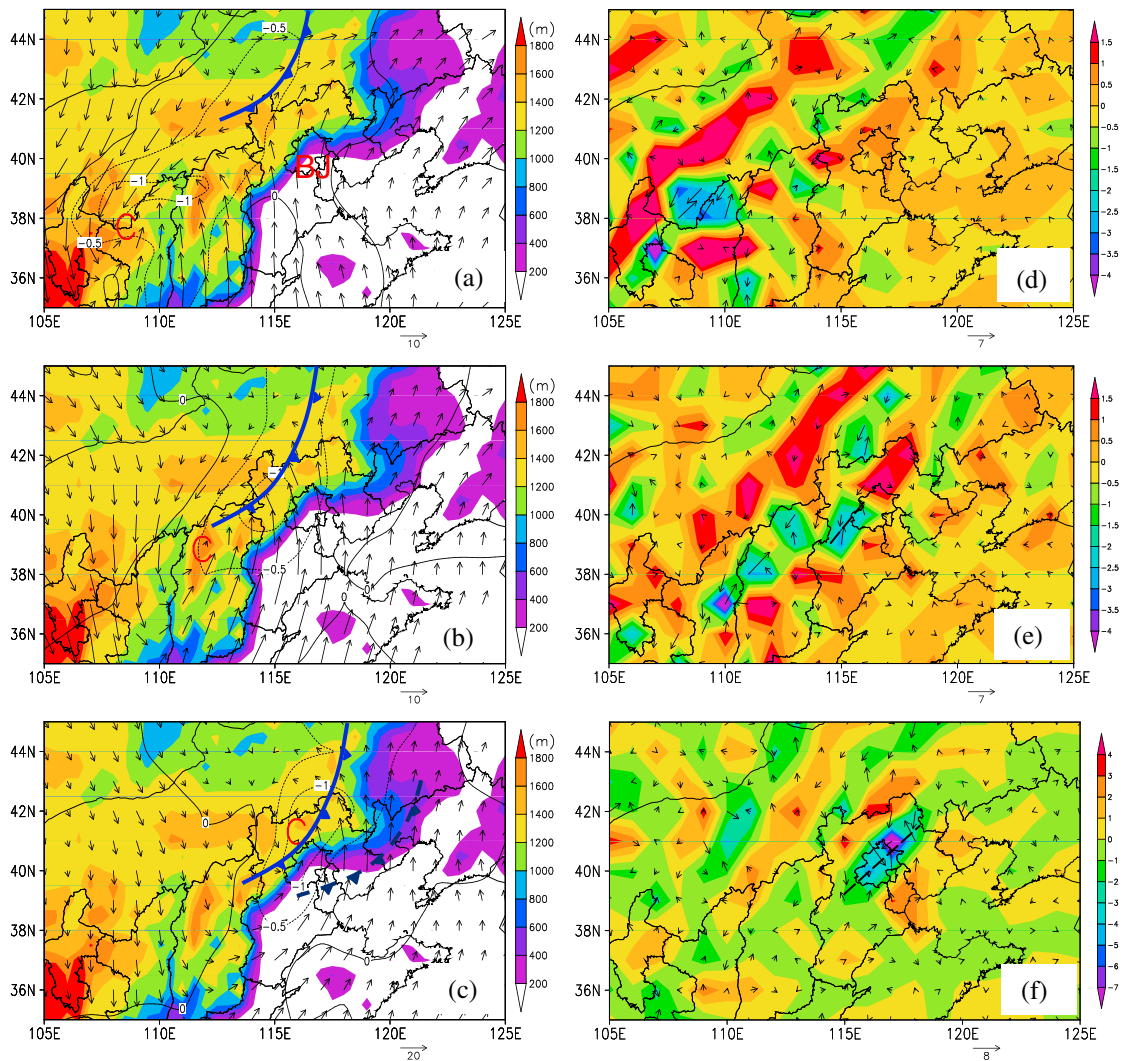


**Figure 4.** Horizontal map of 800 hPa  $\hat{\mathbf{V}}$  (vector;  $\text{m s}^{-1}$ ) and 500 hPa  $\hat{\omega}$  (contour;  $\text{Pa s}^{-1}$ ) from the NCEP final analysis at (a) 0800, (b) 1400, and (c) 2000 BST 21 July 2012, in which topography (m) is shaded; and (d–f) same as in Figures 4a–4c but for 850 hPa  $\mathbf{V}$  ( $\text{m s}^{-1}$ ) and its convergence/divergence (shaded;  $\times 10^{-5} \text{ s}^{-1}$ ). In Figures 4a–4c, letter “C” indicates the cyclone center and blue solid line with arrows denotes the position of a cold front at the surface. In Figure 4a, letters “BJ” indicate the position of Beijing, and in Figure 4c, blue dashed line with arrows is at 0200 BST 22 July. In Figures 4e and 4f, black dashed lines denote a convergence center.

#### 4.1. Synoptic-Scale Background

The previous studies have clearly shown the structures and evolutions of larger-scale atmospheric circulations associated with the Beijing extreme rainfall event [e.g., Sun *et al.*, 2013; Zhang *et al.*, 2013; Ran *et al.*, 2014]. These studies indicated that the extreme rainfall-producing storms were embedded in a large-scale environment with a trough moving southeastward from Lake Baikal, a quasi-stationary subtropical high located between 120°E and 140°E, a cold front at the midlatitudes of East Asia moving eastward, and a lower troposphere cyclonic vortex to the northeast of the Tibetan Plateau moving northeastward. Meanwhile, Beijing was located in the exit region of an upper level jet stream with favorable divergence and was also under the influence of a cold front since 2000 BST 21. Because of the quasi-stationary subtropical high, the approaching trough/cyclone tended to strengthen pressure gradients between the high and the trough and then larger-scale southerly flows ahead of the trough. These results well exhibited a major feature of large-scale atmospheric circulation systems over East Asia during this rainstorm period.

Here we further examine the evolutions of synoptic-scale circulation systems. Figures 4a–4c show the 800 hPa synoptic-scale wind field ( $\hat{\mathbf{V}}$ ). At 0800 BST, a shallow synoptic-scale cyclonic vortex (SCV) appeared

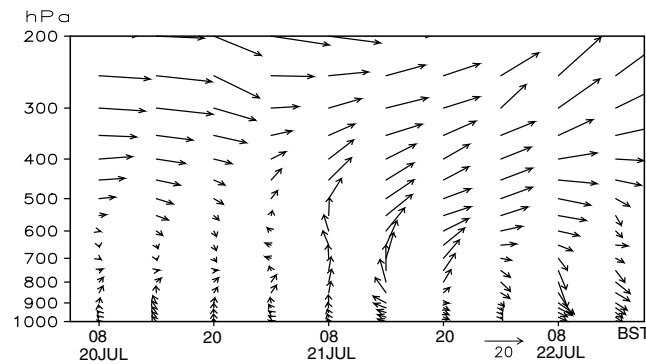


**Figure 5.** Time-height cross section of horizontal wind ( $\text{m s}^{-1}$ ) of the NCEP final analysis at HB from 0800 BST 20 to 1400 BST 22 July.

north of the vortex circulation shown in Figure 4a. The south to southwesterly flows of less than  $8 \text{ m s}^{-1}$  prevailed on the windward side of the southwest-northeast oriented sloping topography over western Beijing and generally went along the topography, not favorable to the development of large upward motion on the windward side.

At 1400 BST, the SCV moved northeastward to  $39^\circ\text{N}/112^\circ\text{E}$  at 800 hPa (Figure 4b), and the cold front was more than 150 km away from Beijing [also see Zhang *et al.*, 2013, Figure 4b]. Strong upward motion of  $1 \text{ Pa s}^{-1}$  associated with SCV also moved northeastward to the west of Beijing. The southeasterly flows above  $10 \text{ m s}^{-1}$  to the northeast of the SCV center prevailed over Beijing and the adjacent areas. At the moment, the southeasterly flows at HB, strongest in the entire rainstorm process, appeared below 700 hPa, with strong southwesterly flows above 700 hPa (Figure 5). At the surface, southeasterly winds above  $4 \text{ m s}^{-1}$  were also observed at Beijing meteorological station (with the identification number of 54511; not shown). These results show that Beijing was located within a warm sector, that is, under the influence of the low-level warm and moist southeasterly flows ahead of both the SCV center and the cold front. Clearly, such strong southeasterly flows would transport abundant water vapor toward Beijing and the adjacent areas, providing a favorable moist environment for the occurrence of heavy rainfall. Large vectors of low-level synoptic-scale water vapor flux ( $q\mathbf{V}_h$ ) toward the northwest appeared near Beijing, indicating strong transport of water vapor (Figure 6a), in which  $q$  is the air specific humidity and  $\mathbf{V}_h$  is the horizontal wind. Large negative values of water vapor flux convergence/divergence ( $\nabla \cdot q\mathbf{V}_h$ ) below  $-2 \times 10^{-7} \text{ s}^{-1}$  covered Beijing, with the central value of  $-5 \times 10^{-7} \text{ s}^{-1}$ , indicating the local strong convergence of water vapor. Meanwhile, the southeasterly flows passed the sloping orographic surface near  $40^\circ\text{N}$  (Figure 4b) and had a larger component perpendicular to the orographic slope compared to the south-southwesterly flows at 0800 BST, which might produce a strong topographic uplift (Figure 7a). Upward motion as large as  $2 \text{ Pa s}^{-1}$  appeared near 800 hPa (Figure 7c). Figure 7d shows a vertical distribution of  $\omega$  driven by the synoptic-scale field at HB at 1400 BST. In this figure,  $\omega$  was weak below 700 hPa and the maximum value of  $-0.67 \text{ Pa s}^{-1}$  appeared near 500 hPa, much smaller than the total  $\omega$  (shown in Figure 7c). This result implied that vertical motion was not mainly driven by the synoptic-scale field at the moment. Thus, the effect of topography on the southeasterly flows possibly played a major role in producing strong upward motion in the lower troposphere. The heaviest rainfall occurred under the warm and moist southeasterly flows during 1300–1400 BST. The first northward propagating strong CR (Figure 3b) coincided well with the northward extension of the southerly wind component.

By 2000 BST, the cold front further approached western Beijing and was located to the west of Beijing (Figure 4c), consistent with the analyses of Zhang *et al.* [2013] and Sun *et al.* [2013]. The SCV center moved close to the north of Beijing, arriving at  $41^\circ\text{N}/116^\circ\text{E}$ . In the surface layer, the southeasterly flows had shifted to northwesterly flows at HB (Figure 5). The easterly wind component below 600 hPa withdrew eastward to  $116^\circ\text{E}$  (Figure 7b). The wind profiler data at  $115.96^\circ\text{E}/40.45^\circ\text{N}$  also showed low-level northerly flows after 1500 BST (not shown). These features indicated the prevalence of northwesterly flows behind the SCV center over Beijing. Large  $q\mathbf{V}_h$  moved eastward and appeared to the east of Beijing, with a  $\nabla \cdot q\mathbf{V}_h$  central value of  $-9 \times 10^{-7} \text{ s}^{-1}$  near Beijing (Figure 6b). Strong upward motion associated with SCV covered

to the northeast of the Tibetan Plateau (Figure 4a), as discussed by Sun *et al.* [2013] and Ran *et al.* [2014]. Its center was located near  $38^\circ\text{N}/108^\circ\text{E}$  at 800 hPa and near  $39^\circ\text{N}/109^\circ\text{E}$  at 700 hPa (not shown), showing a slightly northeastward tilting vertical structure. Meanwhile, the low-level SCV appeared to the south of the 500 hPa large-scale trough (from Lake Baikal). Because no remarkable vortex was observed in the mesoscale wind field ( $\mathbf{V}$ ) (Figure 4d), the vortex shown in Figure 4a exhibited a synoptic-scale feature. At 500 hPa, strong upward motion of  $>1 \text{ Pa s}^{-1}$  appeared in the

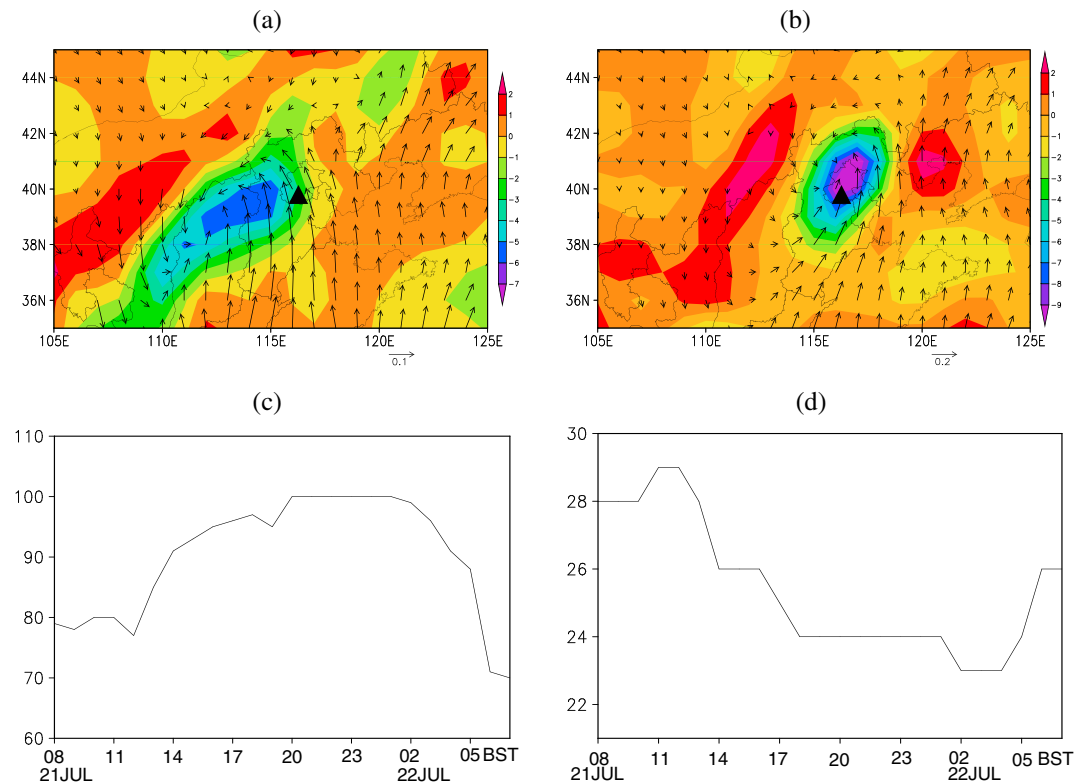


**Figure 6.** Horizontal maps of 850 hPa synoptic-scale water vapor flux ( $\text{m s}^{-1}$ ) and its convergence/divergence (shaded;  $\times 10^{-7} \text{ s}^{-1}$ ) from the NCEP final analysis at (a) 1400 and (b) 2000 BST 21 July 2012, in which the solid and black triangle indicates the position of Beijing meteorological station. (c) Time series of surface air relative humidity (%) at Beijing meteorological station (with the identification number 54511, the latitude/longitude 39.48°N/116.28°E, and the elevation of 31.3 m above the sea level) from 0800 BST 21 to 0700 BST 22 July. (d) Same as in Figure 6c but for surface air temperature (°C).

Beijing (Figure 4c), with upward motion of  $>2 \text{ Pa s}^{-1}$  from the surface layer to 500 hPa (Figure 7c), which indicated deeper upward motion than at 1400 BST. During this process,  $\omega$  driven by the synoptic-scale field significantly strengthened, with the maximum value of  $-1.9 \text{ Pa s}^{-1}$  near 650 hPa (Figure 7d), close to the total  $\omega$  (Figure 7c). This result indicated that vertical motion was mainly driven by the synoptic-scale system. Radar echo propagated southeastward since the later afternoon (in Figure 3). Thus, the occurrence of the evening rainfall was associated with the intrusion of the northwesterly flows behind the approaching SCV center, in contrast to the southeasterly flows in the warm-sector heavy rainfall. After 2000 BST 21, the cold front passed Beijing. It arrived to the east of Beijing at 0200 BST 22 (Figure 4c) and accompanied the third weak rainfall process at HB.

The above results show that the first two heavy rainfall processes occurred ahead of a cold front, and the third weak rainfall process was associated with the passage of the cold front. Here we further examine air relative humidity ( $R$ ) and temperature at the surface at Beijing meteorological station because there is no observation of water vapor at HB. Figure 6c shows the temporal evolution of hourly  $R$  at Beijing station. It is seen that  $R$  rapidly increased from about 80% before 1200 BST to 90% at 1400 BST and reached 100% at 2000 BST 21. From 0100 BST 22, it rapidly decreased. Meanwhile, temperature experienced three decreasing processes (Figure 6d). The first decrease occurred from 1200 to 1400 BST 21, corresponding to the strengthening of synoptic-scale southerly flows and the local heaviest rainfall, which suggests that this decrease in temperature was possibly due to the occurrence of heavy rainfall. The second decrease, also corresponding to the vortex-producing heavy rainfall, was possibly associated with an invasion of the northwesterly flows behind the vortex center as well as the occurrence of heavy rainfall. The third decrease in temperature occurred after 0100 BST 22 July, with a drier surface relative humidity, and accompanied the passage of the cold front after 2000 BST 21, which implied a drier and colder intrusion in the lower troposphere.

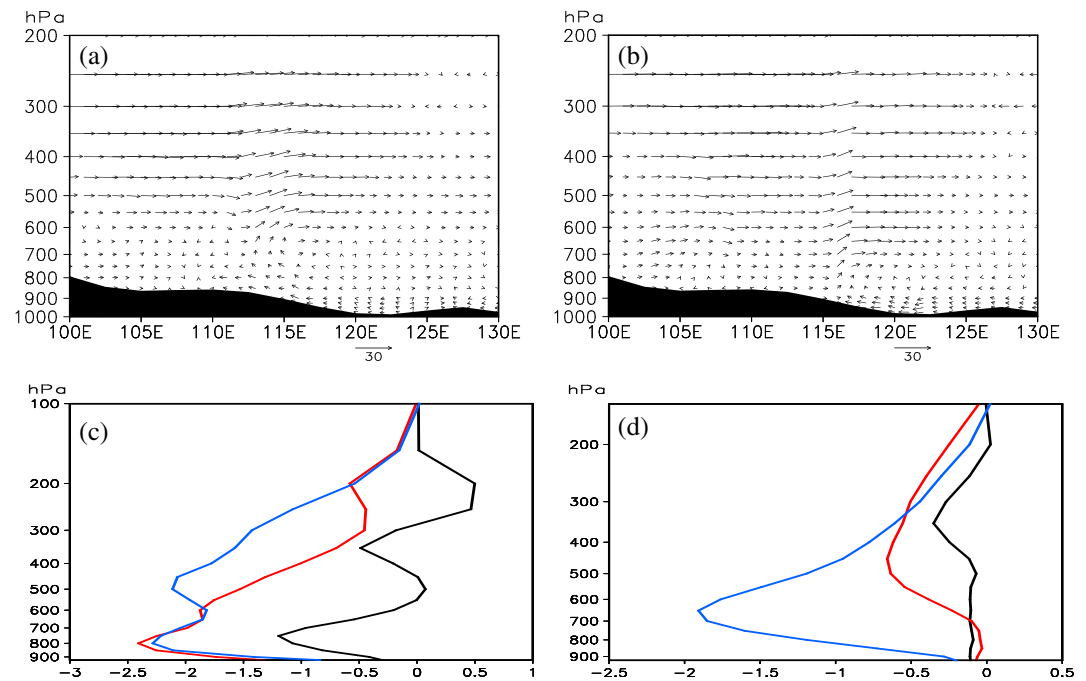


**Figure 7.** (a) Longitude-height cross section of zonal vertical circulation ( $u$ :  $\text{m s}^{-1}$ ;  $p$  velocity:  $\times 0.5 \text{ Pa s}^{-1}$ ) of the NCEP final analysis along  $40^\circ\text{N}$  at (a) 1400 BST 21 July 2012; (b) same as in Figure 7a but for 2000 BST 21 July 2012; (c) vertical distribution of  $p$  velocity ( $\text{Pa s}^{-1}$ ) of the NCEP final analysis at HB at 0800 BST (black), 1400 BST (red), and 2000 BST (blue) 21 July 2012; and (d) same as in Figure 7c but for  $p$  velocity driven by the synoptic-scale field (obtained from quasi-geostrophic  $\omega$  equation).

#### 4.2. Mesoscale Atmospheric Circulations

When warm and moist air masses meet topography, low-level convergence and ascent are often forced on the windward side of sloping topography [Chu and Lin, 2000; Park and Lee, 2007; Houze, 2012]. For this Beijing extreme rainfall event, the dynamic forcing of topography in the west of Beijing to the weak south to southwesterly flows was weak at 0800 BST and no remarkable mesoscale cyclones or mesoscale convergence centers were observed near Beijing (Figure 4d). In contrast, at 1400 BST the strengthened large-scale southeasterly flows had a larger component of climbing the topography (Figure 4b), which might therefore trigger strong mesoscale systems on the windward side. For example, a mesoscale (100 km to 200 km) convergence area, with the central value of  $-2.5 \times 10^{-5} \text{ s}^{-1}$ , was located on the windward side between  $39^\circ\text{N}/114^\circ\text{E}$  and  $40^\circ\text{N}/116^\circ\text{E}$  (Figure 4e), 200 km away from the synoptic-scale vortex center. It is evident that the warm-sector heavy rainfall in this Beijing rainstorm process was closely associated with the large-scale southeasterly flows instead of the southwesterly flows like the warm-sector rainstorms in south China noted by Feng and Luo [1997], Xue [1999], and Zhou *et al.* [2003], which is likely due to the unique topographic forcing near Beijing. Our calculation further shows that the mesoscale convergence ( $\nabla \cdot \mathbf{V}$ ) generally accounted for 50% of the total convergence ( $\nabla \cdot \mathbf{V}$ ) in the surface layer, which suggested the importance of the low-level mesoscale convergence in initiating the local warm-sector convection activities. At 2000 BST, the mesoscale convergence slowly shifted eastward (Figure 4f) and combined with the rapidly moving SCV (Figure 4c).

Because the NCEP final analysis data set has a low temporal/spatial resolution, we follow Sun and Crook [2001] and Xu *et al.* [2006] to analyze finer mesoscale features of the warm-sector rainstorm process using radar-derived wind products with a high horizontal/temporal resolution. Figure 8 shows the derived wind field at the height of 1.5 km away from the elevation of Beijing radar station. Scattered southerly flows were generally weak (below  $8 \text{ m s}^{-1}$ ) before 1200 BST (Figures 8a–8c), accompanied by scattered large values of radar reflectivity in Beijing. At 1200 BST (Figure 8d), easterly or southeasterly flows of larger than  $10 \text{ m s}^{-1}$  appeared near southern Beijing. Afterward, they expanded northward. At 1300 BST (Figure 8e), these flows arrived at  $40^\circ\text{N}$ , with the central value of  $15 \text{ m s}^{-1}$  near  $39.5^\circ\text{N}/116.2^\circ\text{E}$ . Meanwhile, a remarkable mesoscale vortex with a diameter of about 100 km appeared to the southwest of

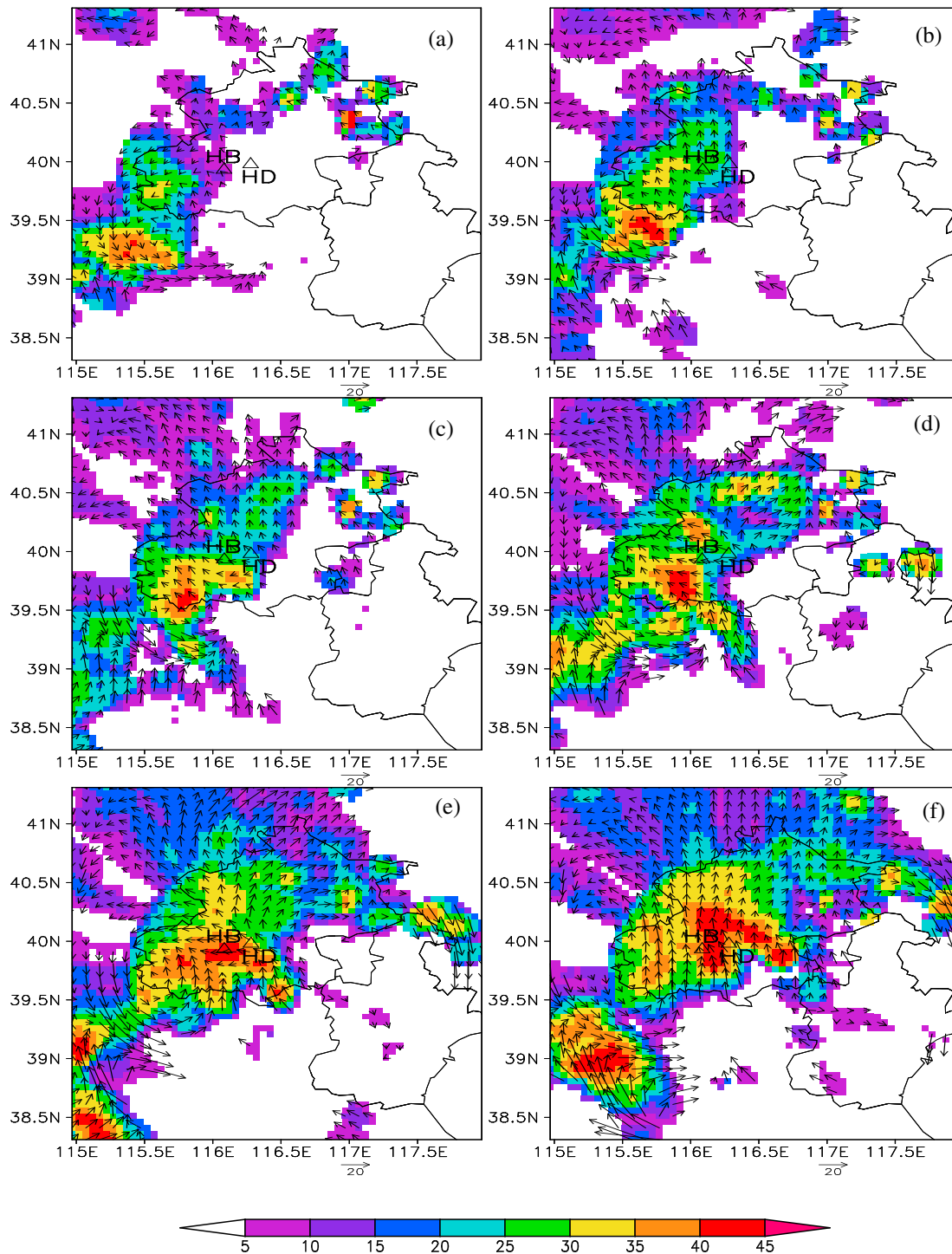


**Figure 8.** The radar-derived wind field ( $\text{m s}^{-1}$ ) and radar reflectivity (dBZ) at the height of 1.5 km away from the elevation of Beijing radar station at (a) 0900, (b) 1000, (c) 1100, (d) 1200, (e) 1300, and (f) 1400 BST 21 July, in which wind arrows and radar reflectivity below 5 dBZ are not plotted.

Beijing (near  $39.8^{\circ}\text{N}/115.5^{\circ}\text{E}$ ), and a convergence area with the central value of  $-6 \times 10^{-4} \text{ s}^{-1}$  (not shown) appeared to the northeast of the mesoscale vortex center. At the moment, large values of radar reflectivity with the central value of  $>40 \text{ dBZ}$  appeared within the easterly or southeasterly flows, corresponding to heavy rainfall above  $20 \text{ mm h}^{-1}$  at HB during 1200–1300 BST (Figure 1c). From 1300 to 1400 BST, one branch of the southerly flows exceeding  $5 \text{ m s}^{-1}$  slightly turned northeastward along the topography near  $40^{\circ}\text{N}/116^{\circ}\text{E}$  and

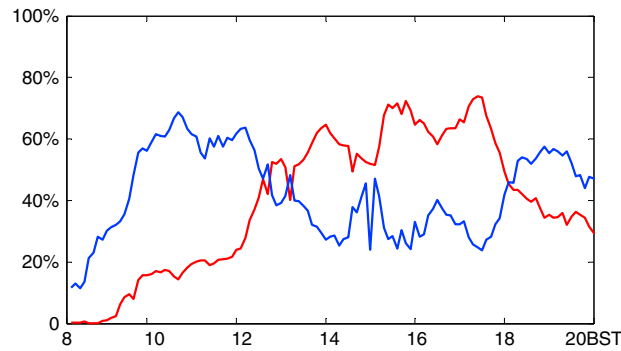


**Figure 9.** Time series of the ratios of convective core (red) and ambient cloud (blue) areas to the total area over a 10 km region of HB from 0800 to 2000 BST 21 July.

met another branch near 40°N/116.7°N (Figures 8e and 8f), which formed convergence centers near western Beijing at 1400 BST (not shown), with strong radar reflectivity of >40 dBZ (Figure 8f). It is evident that the low-level strong southeasterly flows in western Beijing began around 1200 BST and formed low-level mesoscale convergence centers under the influence of the topography. These convergence centers might initiate local convection activities. Afterward, these convergence centers moved toward the east (not shown).

**4.3. Convection Features**

The occurrence of heavy rainfall is usually associated with the development of strong convection. Steiner and Yuter [1995] used radar echo above 40 dBZ to identify convective cores. In China, 38 dBZ can be used as a threshold value [Zhong et al., 2007]. In the present study, we also use 38 dBZ to separate a convective core from its ambient cloud. Figure 9 shows a ratio of the convective core area to the total area over a 10 km region of HB. Generally speaking, when rainfall was weak before 1200 BST, convective cores accounted only for a low ratio (<20%) of the region. The ratio rapidly increased afterward and reached 40–60% during 1300–1400 BST (corresponding to the heavy rainfall at HB). From 1500 BST, it increased once again and exceeded 60% from 1540 to 1730 BST. This feature indicated a larger area of strong convection in the vortex rainstorm process than in the warm-sector process.

To examine the vertical distribution of convective cores, Figure 10a shows the time-height cross section of radar reflectivity at HB. Before 1200 BST, radar reflectivity was weak, generally below 30 dBZ, which indicates weak convection activities. From 1200 BST, radar reflectivity remarkably increased below 6 km and the values of more than 40 dBZ mainly appeared below 4 km. To examine a possible phase of atmospheric water particles, routine radiosonde temperature data at Beijing meteorological station are used to analyze the height of the melting level (or 0°C level). Figure 10b shows the height of the melting level and the vertical distribution of temporal mean radar reflectivity at HB. The mean value between 1230 and 1400 BST exceeded 40 dBZ below 3 km, with the maximum value of 43 dBZ near 1 km (Figure 10b). This suggests convective cores mainly in the lower troposphere. From 1400 to 1500 BST, radar reflectivity rapidly decreased to <30 dBZ. Afterward, it increased once again. The reflectivity below 8 km exceeded 40 dBZ near 1630 BST (Figure 10a). The mean reflectivity value between 1600 and 1900 BST also exceeded 38 dBZ below 4 km, with the maximum value of 41 dBZ near 2 km (Figure 10b). It is evident that convective cores in this period appeared at higher levels compared to the warm-sector process.

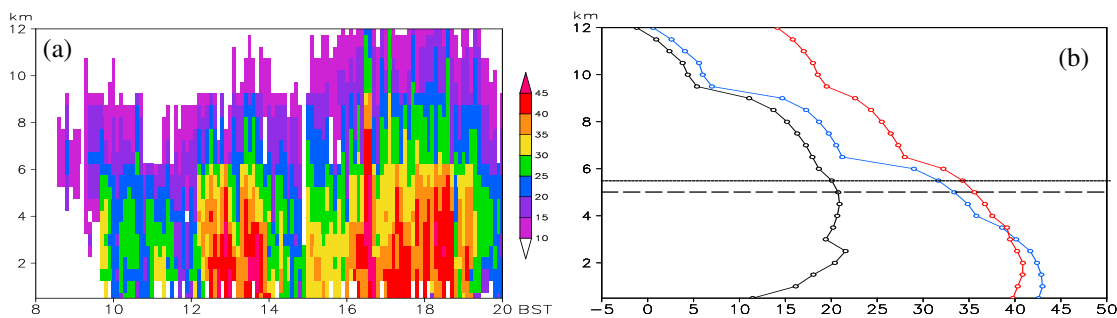


**Figure 10.** (a) Time-height cross section of radar reflectivity (dBZ) at HB from 0800 to 2000 BST 21 July; and (b) same as in Figure 10a but for the temporal mean radar reflectivity during 0900–1100 BST (black), 1230–1400 BST (blue), and 1600–1900 BST (red), in which dashed (dotted) line is for the height of the melting level at 0800 (2000) BST 21 July.

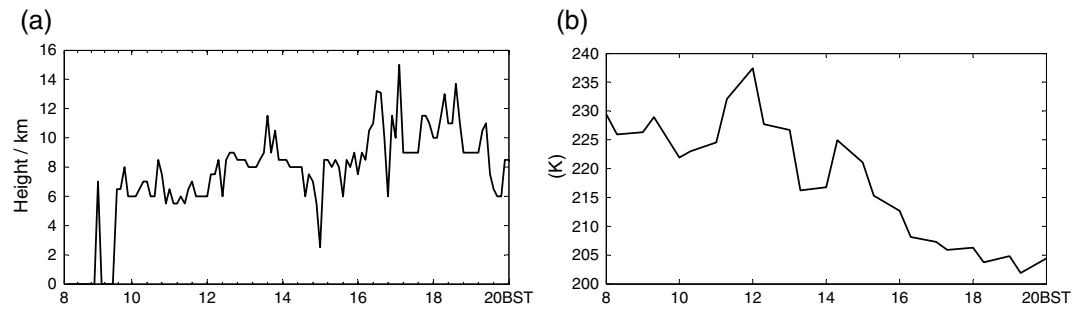


**Figure 11.** Time series of (a) the maximum ET height (km) with a value of  $>18$  dBZ within a 3 km area of HB, and (b) TBB (K) from the Fengyun-2 satellite at HB from 0800 BST to 2000 BST 21 July.

Figure 11a further shows the temporal evolution of the ET height near HB, in which the ET height is defined as the maximum height with a value of  $>18$  dBZ within a 3 km area of HB. It generally showed an increasing trend from 0800 to 2000 BST. ET was generally below 8 km before 1200 BST and exceeded 8 km during 1300–1400 BST, with the maximum height of above 10 km. The second remarkable increase of the ET height occurred near 1500 BST and exceeded 10 km during 1630–1900 BST, with the maximum height of 15 km near 1700 BST. This showed a higher ET in the vortex-producing heavy rainfall process than in the warm-sector heavy rainfall process. The similar feature is seen from TBB (Figure 11b). It generally showed a decreasing trend (that is, an increase of the cloud top height). At 1400 BST, TBB rapidly reduced from 235 K to 215 K. In the evening, TBB further decreased to 205 K near 1800 BST. These results also indicated a higher cloud top in the evening than in the early afternoon.

Summing up, with the low-level SCV moving northeastward from the northeast of the Tibetan Plateau, the strengthened warm and moist southeasterly flows ahead of the SCV center prevailed near Beijing from 1200 to 1500 BST. When they met the sloping topography in the west of Beijing, strong mesoscale convergence and upward motion appeared on the windward side of the topography, with the heaviest hourly rainfall occurring under the southeasterly flows. This process was characterized by a typical feature of warm-sector rainstorms. When the SCV center moved across Beijing, the northwesterly flows behind the center as well as deep upward motion intruded into Beijing, forming the local deep convection and producing the second heavy rainfall in the evening hours. It is noted that compared to the vortex-producing hourly rainfall intensity, the shallower upward motion and convection in the warm sector accompanied the largest hourly rainfall. This result implied the high rainfall efficiency in the warm sector. Then, what factors were possibly responsible for the high rainfall efficiency?

### 5. Some Factors Responsible for the Warm-Sector Largest Rainfall Intensity

In addition to favorable larger-scale forcings, microphysical processes also play important roles in generating heavy rainfall through the formation of cloud water from water vapor and its conversion to precipitation [e.g., Yang and Houze, 1995; Li et al., 2002; Zhu and Zhang, 2006; Huang et al., 2014]. The large amount of water vapor appeared near Beijing in both the early afternoon and the evening and provided a favorable condition for the occurrence of heavy rainfall (shown in Figure 6c). In the following section, we further analyze variations of liquid water (supercooled water and/or ice particles) below (above) the melting level.

The previous study suggested that the radar-derived VIL product with a high temporal and spatial resolution could be a useful tool for assessing the severe weather potential of thunderstorms [Greene and Clark, 1972]. Amburn and Wolf [1997] applied VIL to estimate thunderstorm severity. Here we use the VIL product at Beijing radar station to analyze variations of liquid water during the period of heavy rainfall at HB. Figure 12 shows the time series of VIL from the surface to the melting level near HB. In this figure, VIL was generally smaller before 1230 BST, with values below  $5 \text{ kg m}^{-2}$ . From 1300 to 1400 BST, it exhibited a rapid increase, with an hourly mean value of  $11 \text{ kg m}^{-2}$  and the maximum value of  $18 \text{ kg m}^{-2}$ . This indicated a rapid accumulation of liquid water below the melting level within 1 h and provided more precipitable water, corresponding to the occurrence of the heaviest rainfall. From 1600 to 1900 BST, VIL showed a gradually increasing trend, with a mean value of  $7 \text{ kg m}^{-2}$  during this period, which indicated the relatively weak accumulation of liquid water and provided relatively little precipitable water below the melting level within

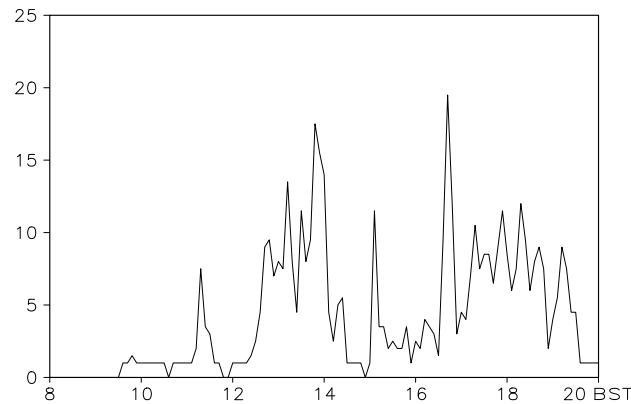


**Figure 12.** Time series of VIL ( $\text{kg m}^{-2}$ ) from the surface to the melting level over a 3 km area of HB from 0800 to 2000 BST 21 July.

1 h. Corresponding to this variation of VIL, the hourly rainfall intensity was relatively weak in the evening but persisted for a long time. The vertical distributions of atmospheric liquid water particles below the melting level and supercooled water and/or ice particles above the melting level are also important factors affecting the rainfall intensity. When these water particles drop in the troposphere, they enter into a higher-temperature environment and have to overcome evaporation produced by a higher environmental temperature. Thus, a large amount of atmospheric water particles favors heavy rainfall to be recorded at the surface. Radar reflectivity in value indicates size and density distributions of atmospheric water particles. Our analysis shows that the melting level was near 5 km (the long dashed line in Figure 10b) at 0800 BST 21 July and near 5.5 km at 2000 BST (the dotted line). This feature indicated a relatively steady height of the melting level between 0800 and 2000 BST. It is seen from Figure 10b that during 0900–1100 BST, the maximum radar reflectivity appeared near the melting level (5.5 km). With the strengthening of upward motion in the troposphere, especially in the lower troposphere (shown in Figure 7c), radar reflectivity below 9 km showed a remarkable increase during 1300–1400 BST (the blue line), especially below the melting level (Figure 10b). This feature indicated a rapid accumulation of atmospheric liquid water particles below the melting level and supercooled water and/or ice particles above the melting level, with the maximum liquid water particles in the surface layer (Figure 10b). A large amount of liquid water particles in the lower troposphere easily overcame evaporation in descent, fell to the ground, and finally produced heavy rainfall, which was consistent with the observational largest rainfall intensity in the warm sector. In the vortex-producing heavy rainfall process, corresponding to the strengthened deep upward motion, radar reflectivity remarkably increased above the melting level (the red line), which implied the great accumulation of supercooled water and/or ice particles there. Compared to lower levels, however, there were stronger horizontal flows at upper levels. Thus, the supercooled liquid water and/or ice particles at upper levels were easily advected downstream, which did not favor the local rainfall production. Meanwhile, radar reflectivity decreased below 3 km, which indicated a decreasing trend of liquid water particles in the lower troposphere (consistent with that in Figure 12), different from the increasing tendency in the warm-sector heavy rainfall process.

Moreover, the evaporation of liquid water particles in descent may cool the unsaturated air, which produces downdrafts and reduces the local rainfall. In Figure 6d, surface air temperature decreased remarkably when the heavy rainfall occurred, from 28°C of the early afternoon to 24°C of the evening. This result implies stronger downdrafts possibly due to the evaporation of liquid water particles in descent in the evening, which may also lead to a weaker rainfall in the vortex-producing heavy rainfall than in the warm-sector rainfall.

Therefore, a large amount of both liquid water particles in the lower troposphere appeared to contribute to the occurrence of the warm-sector largest hourly rainfall. For the vortex-producing heavy rainfall, liquid water particles decreased in the surface layer and there were possibly strong downdrafts due to the evaporation of liquid water particles, which might result in the relatively weak hourly rainfall intensity.

## 6. Summary and Discussion

Using hourly rain gauge data, Doppler radar reflectivity and retrieved horizontal wind, vertical velocity, ET, and liquid water products, satellite TBB products, radiosonde observations, and atmospheric analysis data, we analyze the evolutions of heavy rainfall and radar echo in the Beijing metropolitan area on 21 July 2012 and the variations of synoptic-scale and mesoscale atmospheric circulations and cloud/liquid water. Results show that this rainstorm event occurred as a low-level synoptic-scale vortex from the northeast of the Tibetan Plateau moved, northeastward. A large amount of water vapor transported by the southeasterly flows provided a favorable condition for the occurrence of heavy rainfall. When the

southeasterly flows ahead of the vortex center climbed the sloping topography in the west of Beijing from 1200 to 1400 BST, the dynamic lifting of the topography strengthened local upward motion in the lower troposphere. Meanwhile, one branch of the southeasterly flows turned northeastward along the topography and met another branch near the west of Beijing, which formed mesoscale convergence centers on the windward side of the topography and might produce the heaviest rainfall, with the largest hourly rainfall amount of 86.7 mm. This heavy rainfall event occurred under the low-level warm and moist southeasterly flows and was characterized by a typical feature of the warm-sector rainstorm. With the northward expansion of the southeasterly flows, radar echo also propagated northeastward but persisted for a short period. This warm-sector heavy rainfall in Beijing was closely associated with the southeasterly flows instead of the southwesterly flows like the warm-sector rainstorms in south China. The different scenarios could be attributed to the unique topography near western Beijing.

With the synoptic-scale vortex and associated upward motion approaching Beijing, the southerly flows decreased and the northwesterly flows of the vortex intruded southeastward into Beijing in the evening hours. Compared to the earlier warm-sector rainstorm, in the evening strong upward motion appeared at higher levels due to deep upward motion near the vortex center, with the development of deep convection. When the northwesterly flows expanded southeastward, radar echo propagated systematically southeastward and persisted for a long period, showing an echo training feature noted by Zhang *et al.* [2013]. After the SCV center had passed Beijing, rainfall remarkably decreased.

In the warm-sector rainstorm process, although upward motion and convection were shallow, atmospheric liquid water content in the lower troposphere showed the rapid increase, with the maximum liquid water particles in the surface layer. Large amounts of both liquid water particles in the lower troposphere and supercooled water and/or ice particles above the melting level might be accumulated over the warm sector in one short time. This appeared to contribute to the occurrence of the largest hourly rainfall in the warm sector. In the vortex-producing long-lived rainstorm process, there were deeper strong upward motion and convection, with a larger amount of supercooled water and/or ice particles above the melting level. During this period, however, liquid water decreased in the lower troposphere compared to the early afternoon, and there were possibly strong downdrafts because of the evaporation of liquid water particles in descent, which might result in the relatively weak hourly rainfall. Therefore, low-level liquid water under the warm and moist flows might play more important roles in generating the short-lived heavy rainfall over a warm sector.

Because there were three rainfall stages with different mechanisms in this Beijing rainstorm, the present numerical weather prediction models failed to reproduce three stages, needless to say the location- and magnitude of the extreme rainfall [Zhang *et al.*, 2013]. For example, the operational numerical weather prediction model (T639L60) in the National Meteorological Center of China predicted well the shifts of the cold front and synoptic-scale vortex, the prevalence of southeasterly flows near Beijing, and the frontal rainfall process in Beijing but did not successfully capture the heavy rainfall process (only predicting a small amount of rainfall) over the warm sector in the early afternoon [Zhao *et al.*, 2013]. The Rapid Update Cycle assimilation and forecast system in Beijing Meteorological Bureau also failed to simulate the heavy rainfall process in the early afternoon [Jiang *et al.*, 2014]. Our data analyses suggest that these failures may be partly attributed to the poor prediction of the development of local convergence centers on the windward side of topography over western Beijing and partly to the lack of appropriate cloud/water microphysical processes. Thus, it is needed to systematically examine and improve both the dynamic forcing of the fine topography over western Beijing on southeasterly flows and the microphysical processes of cloud/water for better predicting warm-sector rainstorm processes. It is also necessary to simulate the fine structures of cloud/water and their effects on the extreme rainfall amount in the warm sector as verified against our observational results. These should be addressed in the future work.

#### Acknowledgments

We thank Juazhen Sun of the National Center for Atmospheric Research, Lin Chen of the National Meteorological Satellite Center of China, Xiaoding Yu of the China Meteorological Administration Training Center, and Bai Li of the Meteorological Observation Center of China for their suggestions and constructive comments. The data used to produce the results of this paper can be obtained from Lingzhi Zhong (zhonglz@cams.cma.gov.cn) and Ping Zhao (zhaoping@cams.cma.gov.cn). This study was sponsored by the Third Tibetan Plateau Atmospheric Scientific Experiment (GYHY201406001) and special project of National International Science and Technology Cooperation of China (2011DFG23450).

#### References

- Amburn, S. T., and P. L. Wolf (1997), VIL density as a hail indicator, *Weather Forecasting*, *12*, 473–478.
- Cao, Z. H., and G. W. K. Moore (1998), A diagnostic study of moist potential vorticity generation in an extratropical cyclone, *Adv. Atmos. Sci.*, *15*, 152–166.
- Cao, Z. H., and D. L. Zhang (2005), Sensitivity of cyclone tracks to the initial moisture distribution: A moist potential vorticity perspective, *Adv. Atmos. Sci.*, *22*, 807–820.
- Chen, L. X., Q. G. Zhu, and H. B. Luo (1991), *East Asian Monsoon* [in Chinese], pp. 1–191, Meteorological Press, Beijing.

- Chen, M. X., Y. C. Wang, X. Xiao, and F. Gao (2013), Initial and propagation mechanism for the Beijing heavy rainstorm clusters on July 2012 [in Chinese], *Acta Meteorol. Sin.*, *71*, 569–592.
- Chu, C. M., and Y. L. Lin (2000), Effects of orography on the generation and propagation of mesoscale convective systems in a two-dimensional conditionally unstable flow, *J. Atmos. Sci.*, *57*, 3817–3837.
- Crook, N. A., and J. Sun (2002), Assimilating radar, surface and profiler data for the Sydney 2000 Forecast Demonstration Project, *J. Atmos. Oceanic Technol.*, *19*, 888–898.
- Ding, H. (2004), Seasonal march of the East-Asian summer monsoon, in *East Asian Monsoon*, edited by C. P. Chang, pp. 3–53, World Scientific, Singapore.
- Du, J., R. H. Grumm, and G. Deng (2014), Ensemble anomaly forecasting approach to predicting extreme weather demonstrated by extremely heavy rain event in Beijing [in Chinese], *Chin. J. Atmos. Sci.*, *38*, 685–699.
- Feng, Y. R., and H. B. Luo (1997), On a cumulus convection process in the pre-frontal warm sector over Taiwan area [in Chinese], *Acta Meteorol. Sin.*, *55*, 249–256.
- Gao, S., S. Yang, and B. Chen (2010), Diagnostic analyses of dry intrusion and nonuniformly saturated instability during a rainfall event, *J. Geophys. Res.*, *115*, D02102, doi:10.1029/2009JD012467.
- Greene, D. R., and R. A. Clark (1971), An indicator of explosive development in severe storm, 7th. Con. for Severe Local Storms. Missouri, AMS, 97–104.
- Greene, D. R., and R. A. Clark (1972), Vertically integrated liquid water—A new analysis tool, *Mon. Weather Rev.*, *100*, 548–552.
- Heymsfield, G. M. (1979), Doppler radar study of a warm frontal region, *J. Atmos. Sci.*, *36*, 2093–2107.
- Houze, R. A., Jr. (2012), Orographic effects on precipitating clouds, *Rev. Geophys.*, *50*, RG1001, doi:10.1029/2011RG000365.
- Huang, H.-L., M.-J. Yang, and C.-H. Sui (2014), Water budget and precipitation efficiency of typhoon Morakot (2009), *J. Atmos. Sci.*, *71*, 112–129.
- Huang, S. S., Z. G. Li, and C. L. Bao (1986), *Heavy Rainfalls in the Pre-flood Season in South China* [in Chinese], 1–230, Guangdong Science and Technology Press, Guangzhou.
- Jiang, X. M., H. L. Yuan, M. Xue, X. Chen, and X. G. Tan (2014), Analysis of a torrential rainfall event over Beijing on 21–22 July 2012 based on high-resolution model analyses and forecasts [in Chinese], *Acta Meteorol. Sin.*, *72*, 207–219.
- Jin, L. J., P. R. Li, J. X. Li, H. P. Sun, and Q. J. Feng (2010), Analysis on characteristic of vertically integrated liquid in severe hail shooting process [in Chinese], *Plateau Meteorol.*, *29*, 1297–1301.
- Li, W., D. Z. Jin, J. H. Zheng, D. Z. Tang, M. Z. Liang, Z. X. Chen, and X. G. Wang (2005), Study of expanding the application of VIL [in Chinese], *J. Nanjing Inst. Meteorol.*, *28*, 276–280.
- Li, X., C.-H. Sui, and K.-M. Lau (2002), Dominant cloud microphysical processes in a tropical oceanic convective system: A 2-D cloud resolving modeling study, *Mon. Weather Rev.*, *130*, 2481–2491.
- Luo, Y., Y. Gong, and D. L. Zhang (2014), Initiation and organizational modes in an extreme-rain-producing mesoscale convective system along a Meiyu front in East China, *Mon. Weather Rev.*, *142*, 203–221.
- Maddox, R. A., D. S. Zaras, P. L. Mackeen, J. J. Gourley, R. Rabin, and K. W. Howard (1999), Echo height measurements with the WSR-88D: Use of data from one versus two radars, *Weather Forecasting*, *14*, 455–460.
- Mu, R., L. P. Liu, X. Y. Xu, and W. Zhuang (2007), The capability research on retrieving low-level wind field with 4D-VAR assimilation technique [in Chinese], *Meteorol. Month.*, *33*, 11–18.
- Mu, R., J. Yu, Y. P. Zhang, T. Yi, and Z. J. Li (2012), Radar data analysis and retrieving wind field research of a squall line [in Chinese], *J. Meteorol. Sci.*, *32*, 153–159.
- Nozumi, Y., and H. Arakawa (1968), Prefrontal rain bands located in the warm sector of subtropical cyclones over the ocean, *J. Geophys. Res.*, *73*, 487–492, doi:10.1029/JB073i002p00487.
- Oye, R., C. K. Mueller, and S. Smith (1995), Software for radar translation, visualization, editing, and interpolation, 27th Conference on Radar Meteorology, Vail, Colo., Am. Meteorol. Soc., pp. 359–361.
- Park, S. K., and E. Lee (2007), Synoptic features of orographically enhanced heavy rainfall on the east coast of Korea associated with Typhoon Rusa (2002), *Geophys. Res. Lett.*, *34*, L02803, doi:10.1029/2006GL028592.
- Ran, L. K., Y. B. Qi, and S. C. Hao (2014), Analysis and forecasting of heavy rainfall case on 21 July 2012 with dynamical parameters [in Chinese], *Chin. J. Atmos. Sci.*, *38*, 83–100.
- Robert, A. C., and J. C. Yates (1972), Applications of digital radar data in both meteorology and hydrology, 15th. Con. for Radar Meteor., Urbana, IL, AMS, pp. 93–98.
- Steiner, M., and S. E. Yuter (1995), Climatological characterization of three dimensional storm structure from operational radar and rain gauge data, *J. Appl. Meteorol.*, *34*, 1978–2007.
- Sun, J., and A. Crook (1997), Dynamical and microphysical retrieval from Doppler radar observations using a cloud model and its adjoint: Part I. Model development and simulated data experiments, *J. Atmos. Sci.*, *54*, 1642–1661.
- Sun, J., and A. Crook (1998), Dynamical and microphysical retrieval from Doppler radar observations using a cloud model and its adjoint: Part II. Retrieval experiments of an observed Florida convective storm, *J. Atmos. Sci.*, *55*, 835–852.
- Sun, J., and A. Crook (2001), Real-time low-level wind and temperature analysis using single WSR-88D data, *Weather Forecasting*, *16*, 117–132.
- Sun, J., P. Zhao, and X. J. Zhou (2002), The mesoscale structure of a South China rainstorm and the influence of complex topography [in Chinese], *Acta Meteorol. Sin.*, *60*, 333–342.
- Sun, J., M. X. Chen, and Y. C. Wang (2010), A frequent-updating analysis system based on radar, surface, and mesoscale model data for the Beijing 2008 Forecast Demonstration Project, *Weather Forecasting*, *25*, 1715–1735.
- Sun, J. H., S. X. Zhao, and S. M. Fu (2013), Multi-scale characteristics of record heavy rainfall over Beijing area on July 21, 2012 [in Chinese], *Chin. J. Atmos. Sci.*, *37*, 705–718.
- Tao, S. Y. (1981), *Storm Rainfall in China* [in Chinese], pp. 1–225, Science Press, Beijing.
- Tao, Z. Y., and A. Xie (1989), *Principle and Practice of Weather Process Diagnosis Analysis* [in Chinese], pp. 1–215, Peking Univ. Press, Beijing.
- Xia, R. D., and S. X. Zhao (2009), Diagnosis and modeling of meso- $\beta$ -scale systems of heavy rainfall in warm sector ahead of front in South China (middle part of Guangdong Province) in June 2005 [in Chinese], *Chin. J. Atmos. Sci.*, *33*, 468–488.
- Xia, R. D., S. X. Zhao, and J. H. Sun (2006), A study of circumstances of meso- $\beta$ -scale systems of strong heavy rainfall in warm sector ahead of fronts in South China [in Chinese], *Chin. J. Atmos. Sci.*, *30*, 988–1008.
- Xiao, Y. J., L. P. Liu, and Y. Shi (2008), Study of methods for three-dimensional multiple-radar reflectivity mosaics, *Acta Meteorol. Sin.*, *22*, 351–361.
- Xiao, Y. J., Z. Y. Ma, and Z. H. Li (2009), Advanced algorithms of ET, VIL and density for the CINRAD [in Chinese], *Torrential Rain Disasters*, *28*, 210–214.

- Xu, H. X., X. D. Xu, and S. J. Zhang, and Z. Fu (2014), Long-range moisture alteration of a typhoon and its impact on Beijing extreme rainfall [in Chinese], *Chin. J. Atmos. Sci.*, *38*, 537–550.
- Xu, X. Y., L. P. Liu, and G. G. Zheng (2006), Mesoscale structure of rainstorm retrieved from dual-Doppler radar observations using the 4DVAR assimilation technique, *Acta Meteorol. Sin.*, *20*, 334–351.
- Xue, J. (1999), *Research on Summer Exceptional Rainstorms Over South China in 1994* [in Chinese], pp. 1–185, Meteorological Press, Beijing.
- Yamada, H., B. Geng, and K. K. Reddy (2003), Three-dimensional structure of a mesoscale convective system in a baiu-frontal depression generated in the downstream region of the Yangtze River, *J. Meteorol. Soc. Jpn.*, *81*, 1243–1271.
- Yang, M.-H., and R. A. Houze (1995), Sensitivity of squall line rear inflow to ice microphysics and environmental humidity, *Mon. Weather Rev.*, *123*, 3175–3193.
- Zhang, C. L., B. M. Qian, W. D. He, Y. R. Yang, and Y. H. Lai (2012a), Application of VIL product in high mountain radar [in Chinese], *Plateau Meteorol.*, *31*, 562–567.
- Zhang, D. L., Y. Lin, P. Zhao, X. Yu, S. Wang, H. Kang, and Y. Ding (2013), The Beijing extreme rainfall of 21 July 2012: “Right results” but for wrong reasons, *Geophys. Res. Lett.*, *40*, 1426–1431, doi:10.1002/grl.50304.
- Zhang, J., C. Langston, and K. Howard (2008), Bright band identification based on vertical profiles of reflectivity from the WSR-88D, *J. Atmos. Oceanic Technol.*, *25*, 1859–1872.
- Zhang, J., Y. Qi, D. Kingsmill, and K. Howard (2012b), Radar-based quantitative precipitation estimation for the cool season in complex terrain: Case studies from the NOAA hydrometeorology testbed, *J. Hydrometeorol.*, *13*, 1836–1854.
- Zhang, M., and D. L. Zhang (2012), Sub-kilometer simulation of a torrential-rain-producing mesoscale convective system in East China: Part I. Model verification and convective organization, *Mon. Weather Rev.*, *140*, 184–201.
- Zhang, X. H., and Y. Q. Ni (2009), A comparative study of a frontal and a non-frontal convective systems [in Chinese], *Acta Meteorol. Sin.*, *67*, 108–121.
- Zhang, X. M., W. G. Meng, Y. X. Zhang, and J. Y. Liang (2009), Analysis of mesoscale convective systems associated with a warm sector heavy rainfall event over South China [in Chinese], *J. Trop. Meteorol.*, *25*, 551–560.
- Zhao, P., J. Sun, and X. J. Zhou (2003), Mechanism of formation of low level jets in the South China Sea during spring and summer of 1998, *Chin. Sci. Bull.*, *48*, 1265–1270.
- Zhao, P., R. H. Zhang, J. P. Liu, X. J. Zhou, and J. H. He (2007), Onset of southwesterly wind over Eastern China and associated atmospheric circulation and rainfall, *Clim. Dyn.*, *28*, 797–811.
- Zhao, Y. C., Z. C. Li, and Z. N. Xiao (2008), Comparison analysis of South China front and warm-area heavy rain systems in June 2006 [in Chinese], *Meteorol. Sci. Technol.*, *36*, 47–54.
- Zhao, Y. Y., Q. H. Zhang, Y. Du, M. Jiang, and J. P. Zhang (2013), Objective analysis of the extreme of circulation patterns during the 21 July 2012 torrential rainfall event in Beijing [in Chinese], *Acta Meteorol. Sin.*, *71*, 817–824.
- Zhong, L. Z., L. P. Liu, and S. S. Gu (2007), An algorithm of identifying convective and echo in mixed precipitation and its application in estimating rainfall intensity [in Chinese], *Plateau Meteorol.*, *26*, 593–602.
- Zhou, H. G. (2009), Study mesoscale structure of heavy rainfall on Meiyu front with dual-Doppler radar, *Atmos. Res.*, *93*, 335–357.
- Zhou, H. G., and P. Y. Zhang (2005), A study of the 3D wind of heavy rain with dual-Doppler radar [in Chinese], *Chin. J. Atmos. Sci.*, *29*, 372–386.
- Zhou, T., F. Song, R. Lin, X. Chen, and X. Chen (2013), The 2012 North China floods: Explaining an extreme rainfall event in the context of a long-term drying tendency [in “Explaining Extreme Events of 2012 from a Climate Perspective”], *Bull. Am. Meteorol. Soc.*, *94*, S49–S51.
- Zhou, X. J., et al. (2003), *Experiment and Research on Rainstorm Over South China in 1998* [in Chinese], pp. 1–220, Meteorological Press, Beijing.
- Zhu, T., and D. L. Zhang (2006), Numerical simulation of hurricane bonnie (1998): Part II. Sensitivity to cloud microphysical processes, *J. Atmos. Sci.*, *63*, 109–112.